ISSN 1674-1056
http://cpb.iphy.ac.cn
http://iopscience.iop.org/cpb
中国物理 B
Chinese Physics
中国物理
Chinese Physics B

Electronic states and spin-filter effect in three-dimensional topological insulator Bi_2Se_3 nanoribbons

Genhua Liu(刘根华), Pingguo Xiao(肖平国), Piaorong Xu(徐飘荣), Huiying Zhou(周慧英), Guanghui Zhou(周光辉)
Citation: Chin. Phys. B . 2018, 27(1): 017304. **doi:** 10.1088/1674-1056/27/1/017304

Journal homepage: http://cpb.iphy.ac.cn; http://iopscience.iop.org/cpb

What follows is a list of articles you may be interested in

Quantum spin Hall and quantum valley Hall effects in trilayer graphene and their topological structures

Majeed Ur Rehman, A A Abid
Chin. Phys. B . 2017, 26(12): 127304. **doi:** 10.1088/1674-1056/26/12/127304

Quantum oscillations and nontrivial transport in $(Bi_{0.92}In_{0.08})_2Se_3$

Minhao Zhang(张敏昊), Yan Li(李焱), Fengqi Song(宋凤麒), Xuefeng Wang(王学锋), Rong Zhang(张荣)
Chin. Phys. B . 2017, 26(12): 127305. **doi:** 10.1088/1674-1056/26/12/127305

Topological transport in Dirac electronic systems: A concise review

Hua-Ding Song(宋化鼎), Dian Sheng(盛典), An-Qi Wang(王安琦), Jin-Guang Li(李金光), Da-Peng Yu(俞大鹏), Zhi-Min Liao(廖志敏)
Chin. Phys. B . 2017, 26(3): 037301. **doi:** 10.1088/1674-1056/26/3/037301

Quantum anomalous Hall effect in real materials

Jiayong Zhang(张加永), Bao Zhao(赵宝), Tong Zhou(周通), Zhongqin Yang(杨中芹)
Chin. Phys. B . 2016, 25(11): 117308. **doi:** 10.1088/1674-1056/25/11/117308

Topological hierarchy matters–topological matters with superlattices of defects

Jing He(何敬), Su-Peng Kou(寇谡鹏)
Chin. Phys. B . 2016, 25(11): 117310. **doi:** 10.1088/1674-1056/25/11/117310

Electronic states and spin-filter effect in three-dimensional topological insulator Bi_2Se_3 nanoribbons*

Genhua Liu(刘根华)[1,2,†], Pingguo Xiao(肖平国)[1], Piaorong Xu(徐飘荣)[1], Huiying Zhou(周慧英)[1], and Guanghui Zhou (周光辉)[2]

[1] College of Computer and Information Engineering, Central South University of Forestry and Technology, Changsha 410004, China
[2] Department of Physics and Key Laboratory for Low-Dimensional Quantum Structures and Manipulation (Ministry of Education), Hunan Normal University, Changsha 410081, China

(Received 27 October 2017; published online 28 November 2017)

We study the electronic band structure, density distribution, and transport of a Bi_2Se_3 nanoribbon. We find that the density distribution of the surface states is dependent on not only the shape and size of the transverse cross section of the nanoribbon, but also the energy of the electron. We demonstrate that a transverse electric field can eliminate the coupling between surface states on the walls of the nanoribbon, remove the gap of the surface states, and restore the quantum spin Hall effects. In addition, we study the spin-dependent transport property of the surface states transmitting from top and bottom surfaces (x–y plane) to the side surfaces (z–x plane) of a Bi_2Se_3 nanoribbon. We find that transverse electric fields can open two surface channels for spin-up and -down Dirac electrons, and then switch off one channel for the spin-up Dirac electron. Our results may provide a simple way for the design of a spin filter based on topological insulator nanostructures.

Keywords: topological insulator, Bi_2Se_3 nanoribbon, density distribution, electronic transport

PACS: 73.20.–r, 73.20.At, 73.22.–f, 73.23.-b **DOI:** 10.1088/1674-1056/27/1/017304

1. Introduction

In recent years, a new class of materials called topological insulators (TIs) has generated a great deal of interest, which are in a new quantum substance state originating from spin–orbit coupling (SOC) characterized by spin polarized helical boundary states.[1,2] TIs exhibit many new quantum effects[3–12] and may be extensively used in spintronic devices with high speed and low consumption as well as quantum information processing. However, the above properties can be realized only in an idealized situation. TI samples occupy only a finite space in reality, and also have a variety of shapes surrounded generally by a curved or folded surface(s). Due to the up-to-date semiconductor technologies, high-quality Bi_2Se_3 thin films,[13,14] nanoribbons, and nanowires[15–17] have been fabricated, which have stimulated many theoretical works.[18–24] With the decrease of the films thickness, the surface states on the top and bottom surfaces couple together to produce a gap in the spectrum.[18] Subsequently, this gap was experimentally observed by angle-resolved photoemission spectroscopy,[25] and was found to be tunable by a back gate in Sb_2Te_3 thin films.[26] Similarly, Bi_2Se_3 nanoribbons and nanowires also exhibit a clear gap of surface states in some nanometer scale size.[22,23] This mechanism, to open a gap in the surface electronic spectrum, is spin-to-surface locking and mixing of the surface electronic wave functions.[27] The gaps indicate that some properties of the helical surface states are destroyed. For all that, with their large surface-to-volume ratios, TI nanoribbons are expected to significantly enhance surface conduction, and also enable surface manipulation by external means. The reason is that it has been difficult to modulate surface conduction because of the dominant bulk contribution due to impurities and thermal excitations in the small-band gap bulk material.[28,29] Therefore, it is very important to remove the gap and restore the quantum spin-Hall effect in a TI nanoribbon before its applications in nanoelectronics and spintronics. In addition, these nanoribbons pose many interesting questions concerning the properties of the surface states on the wall surfaces. For instance, since there are four wall surfaces for a rectangular prism-shaped nanoribbon, how do the spin-dependent surface states couple and decouple each other at the four wall surfaces? The transport property of surface states between the walls in the presence of electric fields is also a very interesting problem. It is the purpose of this paper to report systematic theoretical investigations of surface states in Bi_2Se_3 nanoribbons.

In this work, we study the band structure, surface-state density distribution, and electronic transport of nanoribbons. We find that a gap is opened by the coupling of the surface states between the walls of the nanoribbon. We demonstrate that an appropriate electric field can remove the coupling of surface states, close the gap, and restore the quantum spin Hall effects. We also find that the distribution of the surface states is dependent on the shape and size of the transverse cross section,

*Project supported by the National Natural Science Foundation of China (Grant Nos. 11547051 and 11274018).
†Corresponding author. E-mail: genhualiu2006@126.com
© 2018 Chinese Physical Society and IOP Publishing Ltd

and the energy of the electron. In addition, we study the spin-dependent transport property of the surface states transmitting from top and bottom surfaces (x–y plane) to left and right side surfaces (z–x plane) of a Bi_2Se_3 nanoribbon. We demonstrate that the transverse electric field E_y can switch on/off the charge channels of surface states in the nanoribbon. When the channels are just switched on by the electric field E_y, both spin-up and -down electrons can pass through the channels. However, with the increase of the electric field, only spin-down electrons of the surface states can pass through nanoribbon. Unlike in a conventional spin transistor, the spin filtering effect does not rely on a tunable Rashba SOC, but on the energy dependence of the edge state.

2. Theoretical method

In our analysis, we use an effective four-band model[30] that depicts low-energy physics of three-dimensional (3D) TI materials like Bi_2Se_3 centered around the Γ-point in the Brillouin zone, and the Hamiltonian is given by

$$H_{3D} = \begin{bmatrix} \varepsilon_k + M(k) & -iA_1\partial_z & 0 & A_2k_- \\ -iA_1\partial_z & \varepsilon_k - M(k) & A_2k_- & 0 \\ 0 & A_2k_+ & \varepsilon_k + M(k) & iA_1\partial_z \\ A_2k_+ & 0 & iA_1\partial_z & \varepsilon_k - M(k) \end{bmatrix}, \quad (1)$$

where $\varepsilon_k = C - D_1\partial_z^2 + D_2(k_x^2 - \partial_y^2)$, $M(k) = M + B_1\partial_z^2 - B_2(k_x^2 - \partial_y^2)$, and $k_\pm = k_x \pm \partial_y$. The parameters in the model have been obtained by fitting the Bi_2Se_3 band structure from first-principles calculation:[30] $C = -6.8 \times 10^{-3}$ eV, $M = 0.28$ eV, $A_1 = 2.2$ eV·Å, $A_2 = 4.1$ eV·Å, $B_1 = 10$ eV·Å^2, $B_2 = 56.6$ eV·Å^2, $D_1 = 1.3$ eV·Å^2, and $D_2 = 19.6$ eV·Å^2. In the presence of an external electric field $\mathbb{E}_z$ (or $\mathbb{E}_y$) along the z (or y) direction, the total Hamiltonian is

$$H = H_{3D} + V, \quad (2)$$

where $V = e\varepsilon_0/(\varepsilon_0+\varepsilon_r)\mathbb{E}_z \cdot \boldsymbol{z} = e\boldsymbol{E}_z \cdot \boldsymbol{z}$ or $V = e\varepsilon_0/(\varepsilon_0+\varepsilon_r)\mathbb{E}_y \cdot \boldsymbol{y} = e\boldsymbol{E}_y \cdot \boldsymbol{y}$ is a potential energy induced by electric field $\mathbb{E}_z$ along the z direction or $\mathbb{E}_y$ along the y direction respectively, $\boldsymbol{E}_z$ and $\boldsymbol{E}_y$ are two effective electric fields which are respectively produced by $\mathbb{E}_z$ and $\mathbb{E}_y$ in the nanoribbon with dielectric constant ε_r, ε_0=1 for the air environment. For a Bi_2Se_3 nanoribbon with a rectangular cross section, the total envelope function can be written in the form

$$\psi(x,y,z) = e^{ik_x x}\sum_{m,n}\chi_{m,n}\phi_m(z)\phi_n(y). \quad (3)$$

Here $\chi_{m,n}$ is a 4×1 matrix, $\phi_m(z) = \sqrt{2/L_z}\sin\frac{m\pi}{L_z}(z+L_z/2)$, and $\phi_n(y) = \sqrt{2/L_y}\sin\frac{n\pi}{L_y}(y+L_y/2)$, where L_z and L_y are the thickness and width of the nanoribbon, and $n,m = 1,2,\ldots,N$. The number N here must be large enough to obtain a convergent numerical result. Using the above envelope function (3), we can derive the matrix elements of the Hamiltonian, and obtain the band structure and wave functions of the system. Then we are able to study the spin-polarized electron transport of the nanoribbon using a transfer matrix approach.[31,32]

3. Results and discussion

In what follows, we present some numerical results for a rectangular-prism shaped Bi_2Se_3 nanoribbon. Figure 1(a) shows the electronic band structure of the Bi_2Se_3 nanoribbon with $L_z = L_y = 10$ nm in the absence of an electric field. The surface states open a gap ε_g due to the effect of finite size, such as the coupling between the surface states on the walls surface. In order to remove the gap, we apply a transverse electric field to modulate the SOC in the nanoribbon, and remove the coupling between the surface states. In Figs. 1(b) and 1(c), we plotted the band structures of the nanoribbon in the presence of electric fields $E_z = 3.75 \times 10^7$ V/m and $E_y = 2.7 \times 10^7$ V/m, respectively. The two figures show that the energy gap is removed by a sufficient high transverse electric field E_z or E_y, while the gap can be more easily removed by E_y than E_z. The reason is that E_y and E_z break the spatial-inversion symmetry along the y and z directions, respectively, which results in a difference of SOC in the Bi_2Se_3 crystal with an anisotropic lattice structure.

In addition, all electron states are split into doublets due to the Rashba spin–orbit interaction induced by the transverse electric field. Figure 1(d) shows the gap ε_g as a function of L_z (where $L_z = L_y$) for a Bi_2Se_3 nanoribbon without an electric field. The ε_g decreases with the increase of L_z. Particularly, at the value of $L_z = 58$ nm, the gap ε_g closes. The inset of Fig. 1(d) shows the gap ε_g as a function of an electric field E_z or E_y for the nanoribbon with $L_y = L_z = 10$ nm. The two transverse electric fields can change the energy gap of the nanoribbon. With the increases of E_z or E_y, the gap ε_g decreases, and can be removed when these electric fields are sufficiently high. We also note that the gap can be more easily removed by E_y than E_z due to the Bi_2Se_3 crystal with anisotropic lattice structure. When the electric fields further increase, the gaps can be reopened as a result of the interaction between the intrinsic SOC in the nanoribbon and the extrinsic Rashba SOC.

Now, we investigate the density distributions of the lowest electron states marked with a number $n = 1$ (blue solid line in Fig. 1) in prism-shaped nanoribbons without an electric field. Figure 2 shows that the density distributions $|\psi_{\uparrow\downarrow}(k_{x\downarrow,\uparrow},z,y)|^2_{n=1}$ of a Bi_2Se_3 nanoribbon with $L_z = L_y = 5$, 7, 10, 20, 40, 60, 80, and 100 nm, respectively. Here we set the spin-up and -down wave vectors $k_{x\downarrow,\uparrow} = 10^8$ m^{-1}. We find that the densities $|\psi_{\uparrow\downarrow}(k_{x\downarrow,\uparrow},z,y)|^2_{n=1}$ distribute at the center of the nanoribbon when the acreage of the transverse cross section of the nanoribbon is sufficiently small, such as $L_z = L_y = 5$ nm.

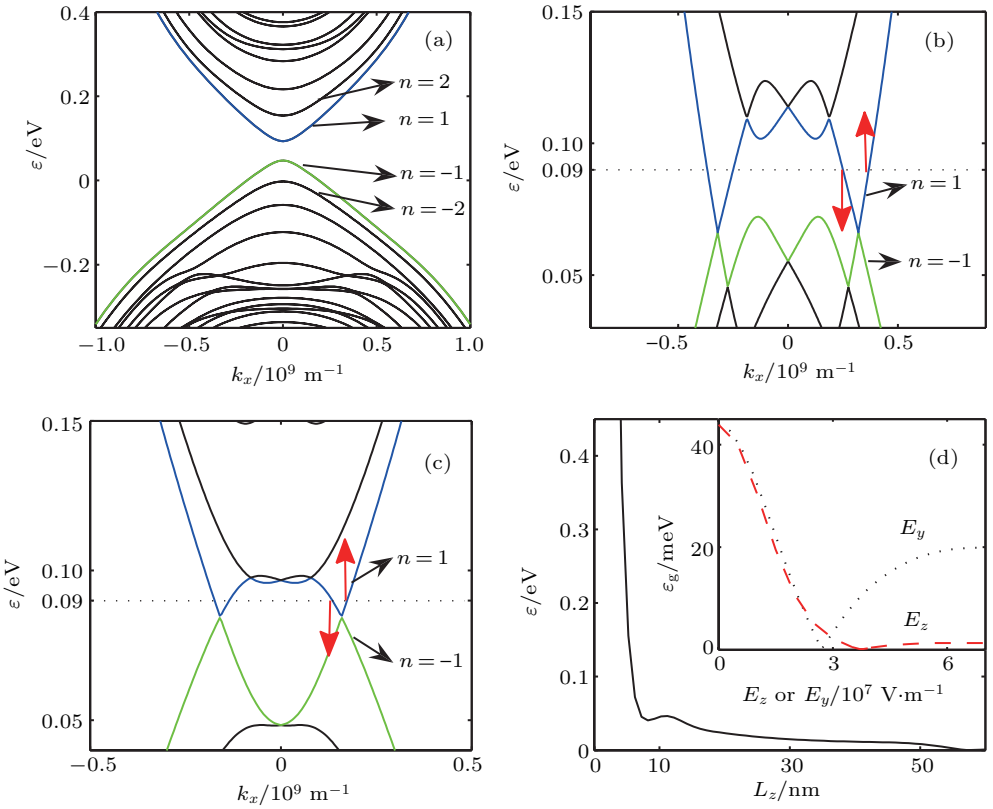


Fig. 1. (color online) Energy band structure for a Bi_2Se_3 nanoribbon with $L_y = L_z$=10 nm under an electric field with strength (a) 0, (b) $E_z = 3.75 \times 10^7$ V/m, and (c) $E_y = 2.7 \times 10^7$ V/m. (d) The band gap ε_g as a function of L_z ($L_z = L_y$). The inset shows ε_g vs E_y (black dotted line) and E_z (red dash line). Spin-up and -down surface states are marked with up and down red arrows in panels (b) and (c), respectively.

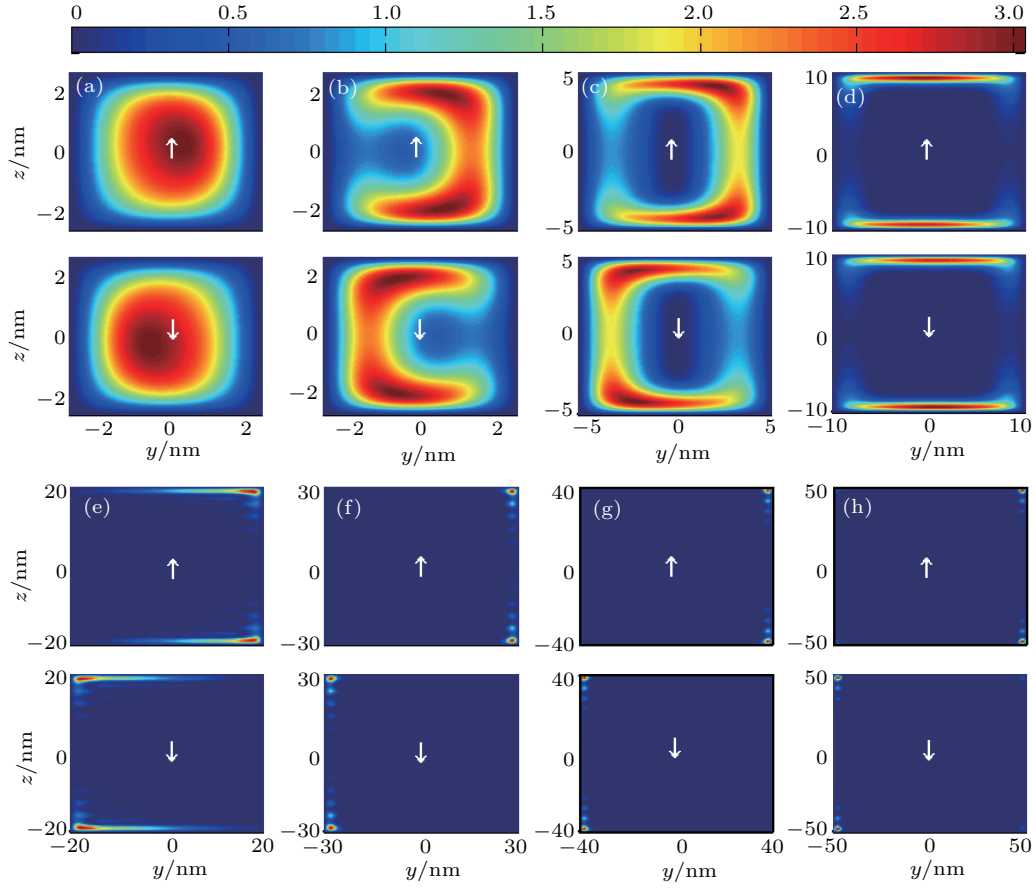


Fig. 2. (color online) Contour plot of the density distributions $|\psi_{\uparrow\downarrow}(k,z,y)|^2_{n=1}$ of the electron states ($n = 1$) for square cross sections of Bi_2Se_3 nanoribbons with $L_z = L_y =$ (a) 5, (b) 7, (c) 10, (d) 20, (e) 40, (f) 60, (g) 80, and (h) 100 nm. ↑ and ↓ stand for spin-up and -down surface states, respectively.

It indicates that the nanoribbon is not a TI but a semiconductor. With the increase of the acreage of the transverse cross section, the densities $|\psi_{\uparrow\downarrow}(k_{x\uparrow,\downarrow},z,y)|^2_{n=1}$ gradually shift from center to surfaces, and gradually gather at both the top and bottom surfaces (x–y planes) as shown in Figs. 2(a)–2(d). With further increasing the acreage of the transverse cross section, the densities $|\psi_{\uparrow}(k_{x\uparrow},z,y)|^2_{n=1}$ and $|\psi_{\downarrow}(k_{x\downarrow},z,y)|^2_{n=1}$ gradually gather themselves to the opposite two pair arris of the nanoribbon, respectively. Figures 2(d)–2(h) show that the wave function of the spin-up and -down surface states are gradually separated. When the transverse cross-section of the nanoribbon is large enough, such as $L_z = L_y = 60$ nm, the densities $|\psi_{\uparrow\downarrow}(k_{x\downarrow,\uparrow},z,y)|^2$ almost locate at the opposite two pair arris of the nanoribbon. Such a spatial separation suppresses back scattering by minimizing the coupling between spin-up and spin-down electron states, which exhibits the property of 3D TI helical surface states.[33]

In Fig. 3, we plot the density distributions of the spin-up and -down electron states marked with $n = -1$ (green solid line in Fig. 1) in prism-shaped nanoribbons. We also set the spin-up and -down wave vectors $k_{x\downarrow,\uparrow} = 10^8$ m^{-1}. When the acreage of the transverse cross section is sufficiently small, the densities $|\psi_{\uparrow\downarrow}(k_{x\downarrow,\uparrow},z,y)|^2_{n=-1}$ distribute at the center of the nanoribbon, the same as the densities $|\psi_{\uparrow\downarrow}(k_{x\downarrow,\uparrow},z,y)|^2_{n=1}$. With the increase of L_y and L_z, the densities $|\psi_{\uparrow\downarrow}(k_{x\uparrow,\downarrow},z,y)|^2_{n=-1}$ also shift from center to side surfaces. But the densities $|\psi_{\uparrow}(k_{x\uparrow},z,y)|^2_{n=-1}$ only gradually gather at the left wall surface (z–x plane) of the nanoribbon, and the densities $|\psi_{\downarrow}(k_{x\downarrow},z,y)|^2_{n=-1}$ only gradually gather at the right wall surface (z–x plane) of the nanoribbon, as shown in Figs. 3(b)–3(h), indicating that the wave function of the spin-up and -down surface states are completely separated, which means the densities $|\psi_{\uparrow}(k_{x\uparrow},z,y)|^2_{n=-1}$ and $|\psi_{\downarrow}(k_{x\downarrow},z,y)|^2_{n=-1}$ are easier to be separated than the densities $|\psi_{\uparrow}(k_{x\uparrow},z,y)|^2_{n=1}$ and $|\psi_{\downarrow}(k_{x\downarrow},z,y)|^2_{n=1}$ in a nanoribbon. So appropriate Fermi energy is necessary for electrons in nanoribbons to exhibit the helical property of TI surface states.

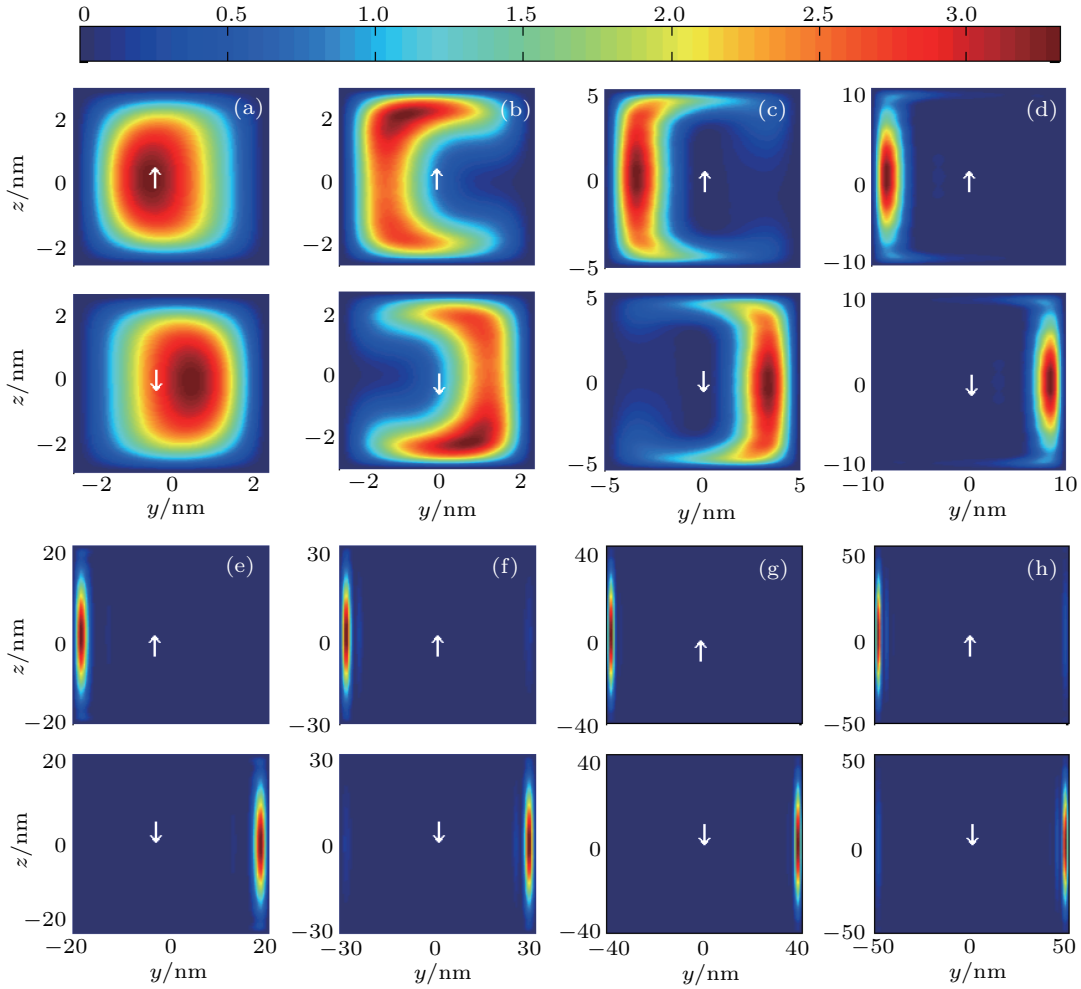


Fig. 3. (color online) Contour plot of the density distributions $|\psi_{\uparrow\downarrow}(k,z,y)|^2_{n=-1}$ of the electron states ($n = -1$) for square cross sections of Bi_2Se_3 nanoribbons with $L_z = L_y =$ (a) 5, (b) 7, (c) 10, (d) 20, (e) 40, (f) 60, (g) 80, and (h) 100 nm, respectively.

We also plot the density distributions of nanoribbons with a rectangular cross section in Figs. 4 and 5. We set the nanoribbon with a fixed thickness $L_z = 10$ nm and different widths $L_y = 4$, 8, 22, 50, 60, 80, 90, and 120 nm in both figures. In addition, we also set the spin-up and -down wave vectors $k_{x\downarrow,\uparrow} = 10^8$ m^{-1}. Firstly, we analyze the density distributions $|\psi_{\uparrow\downarrow}(k_{x\downarrow,\uparrow},z,y)|^2_{n=1}$ shown in Fig. 4. When L_y is sufficiently small, such as 4 nm, the densities $|\psi_{\uparrow\downarrow}(k_{x\downarrow,\uparrow},z,y)|^2_{n=1}$ distribute at the center of the nanoribbon. With the increase of the width L_y, the densities gradually shift from the center to the top and bottom wall surfaces (x–y plane). We also find that most of the densities $|\psi_{\uparrow}(k_{x\uparrow},z,y)|^2_{n=1}$ and $|\psi_{\downarrow}(k_{x\downarrow},z,y)|^2_{n=1}$ gradually gather at both top and bottom surfaces, and the spin-up and -down surface states overlap each other at the two surfaces. When $L_y = 50$ nm, the densities $|\psi_{\uparrow}(k_{x\uparrow},z,y)|^2_{n=1}$ and $|\psi_{\downarrow}(k_{x\downarrow},z,y)|^2_{n=1}$ are completely separated, and respectively distribute at bottom and top wall surfaces. Further increasing the width L_y, the separation alternates with the overlap of the spin-up and -down densities $|\psi_{\uparrow\downarrow}(k_{x\downarrow,\uparrow},z,y)|^2_{n=1}$ (see Figs. 4(e)–4(h)).

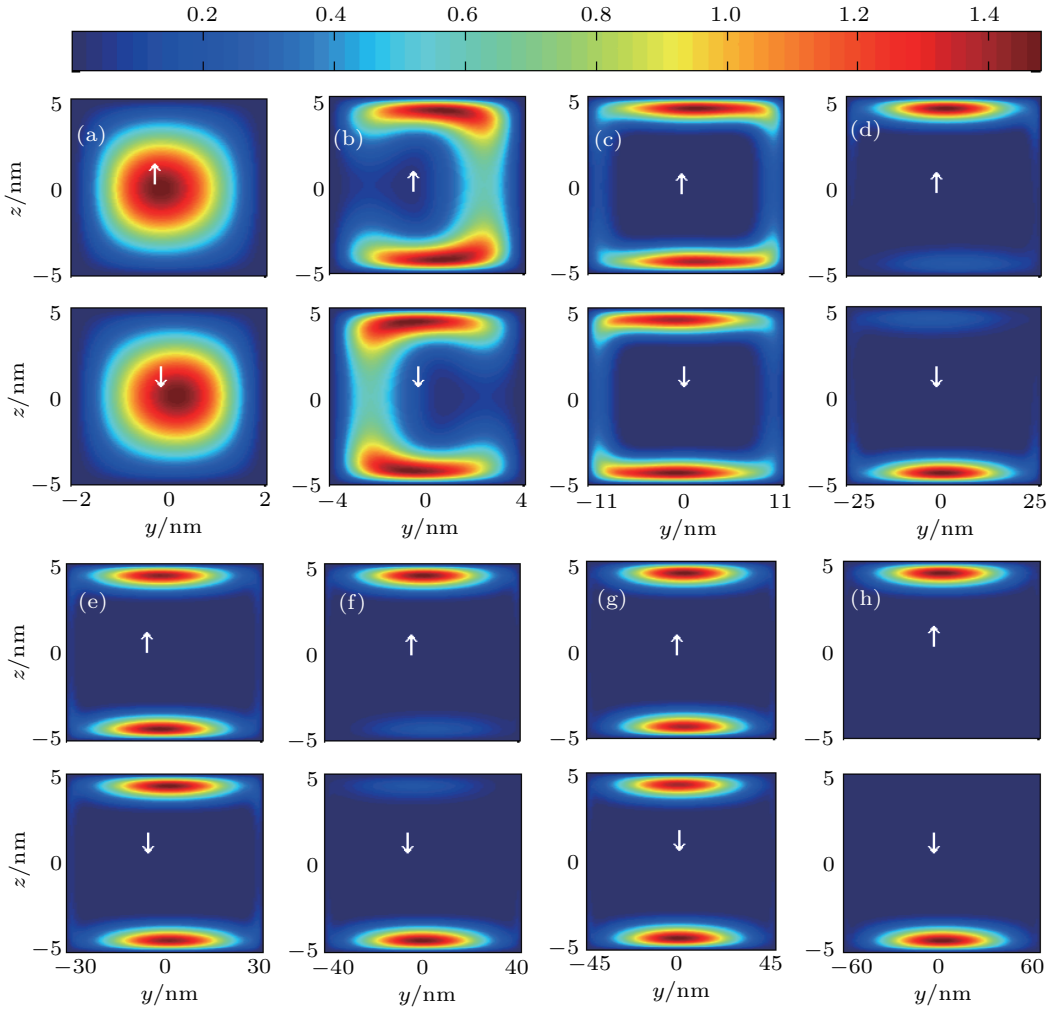


Fig. 4. (color online) Contour plot of the density distributions $|\psi_{\uparrow\downarrow}(k,z,y)|^2_{n=1}$ for rectangular cross sections of Bi_2Se_3 nanoribbons with $L_z = 10$ nm and $L_y =$ (a) 4, (b) 8, (c) 22, (d) 50, (e) 60, (f) 80, (g) 90, and (h) 120 nm, respectively.

Secondly, we discuss the densities distribution of the electron states marked with $n = -1$ (or below the Dirac cone) of the nanoribbon, as shown in Fig. 5. When the width L_y is sufficiently small, the densities $|\psi_{\uparrow}(k_{x\uparrow},z,y)|^2_{n=-1}$ and $|\psi_{\downarrow}(k_{x\downarrow},z,y)|^2_{n=-1}$ also distribute at the center of the nanoribbon. With the increase of the width L_y, the densities $|\psi_{\uparrow}(k_{x\uparrow},z,y)|^2_{n=-1}$ and $|\psi_{\downarrow}(k_{x\downarrow},z,y)|^2_{n=-1}$ gradually shift from center to the left and right side surface (z–x plane), respectively. So the coupling between the spin-up and -down electron states marked with $n = -1$ gradually decrease. When the width L_y is large enough, the density $|\psi_{\uparrow}(k_{x\uparrow},z,y)|^2_{n=-1}$ only gathers at the left side surface, and the other density $|\psi_{\downarrow}(k_{x\downarrow},z,y)|^2_{n=-1}$ only gathers at the right side surface. Therefore, the spin-up density $|\psi_{\uparrow}(k_{x\uparrow},z,y)|^2_{n=-1}$ and spin-down density $|\psi_{\downarrow}(k_{x\downarrow},z,y)|^2_{n=-1}$ are completely separated in the naroribbon with a large width (see Figs. 5(d)–5(h)), indicating that there is no coupling between the spin-up and -down electron states marked with $n = -1$. In addition, these electron states exhibit the properties of the two-dimensional TI, the same as the edge states in HgTe/CdTe quantum well.

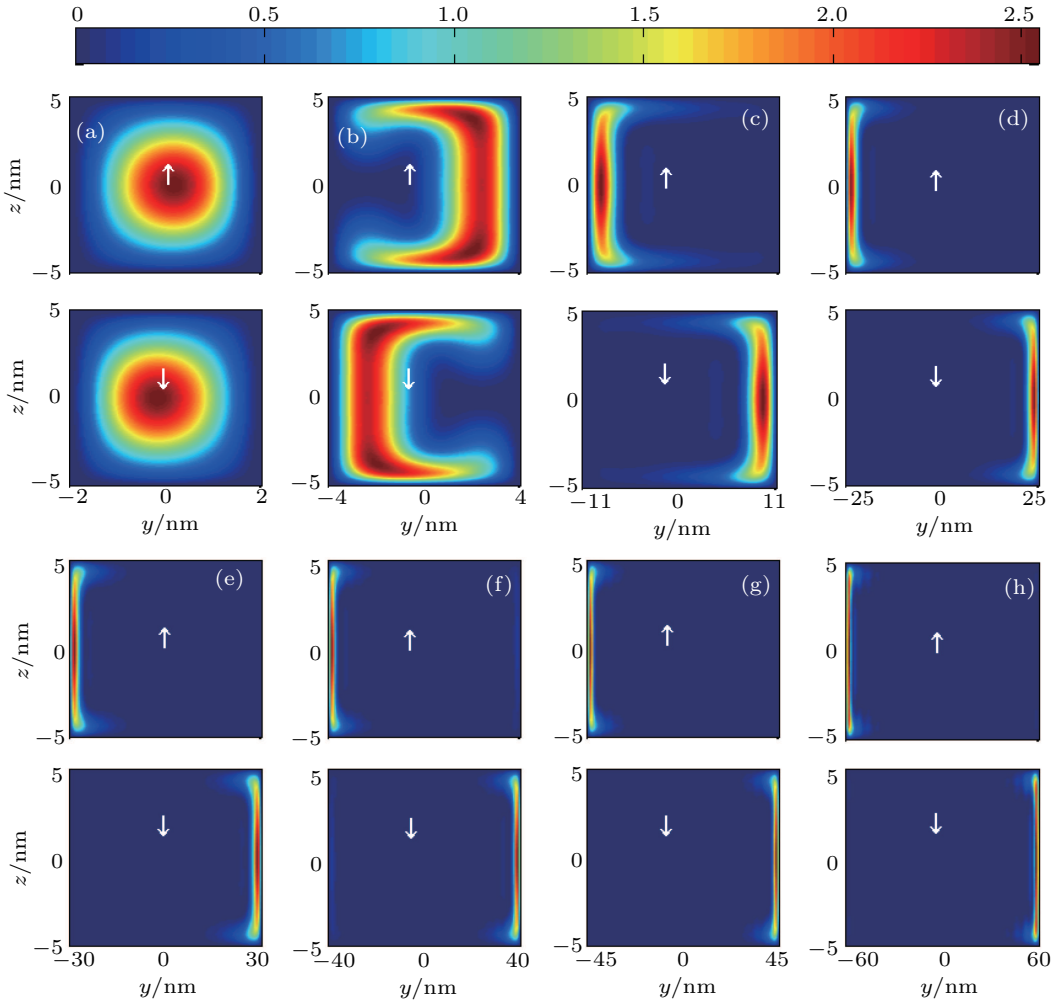


Fig. 5. (color online) Contour plot of the density distributions $|\psi_{\uparrow\downarrow}(k,z,y)|^2_{n=-1}$ for rectantgular cross sections of Bi_2Se_3 nanoribbons with $L_z = 10$ nm and $L_y =$ (a) 4, (b) 8, (c) 22, (d) 50, (e) 60, (f) 80, (g) 90, and (h) 120 nm, respectively.

In order to understand the effect of the transverse electric field on the electron states marked with $n = 1$, we firstly plot the densities $|\psi_{\uparrow\downarrow}(k_{x\downarrow,\uparrow},z,y)|^2_{n=1}$ (where $k_{x\downarrow,\uparrow} \geq 0$ and the electron energy $\varepsilon = 90$ meV) of a nanoribbon with $L_z = L_y =$ 10 nm under a transverse electric field $E_z = 1\times10^7$, 2×10^7, 3.75×10^7, and 5×10^7 V/m, respectively. The electric field E_z along the z direction is applied perpendicularly to both the top and bottom wall surface (x–y plane). In addition, we set the electronic energy $\varepsilon = 90$ meV, which is just in the gap as shown in Fig. 1(a), indicating that there is no electronic state without an external electric field. So the transverse electric field E_z is necessary to stimulate electron states at the energy. We plot the densities $|\psi_{\uparrow\downarrow}(k_{x\downarrow,\uparrow},z,y)|^2_{n=1}$ of the states stimulated by an electric field $E_z = 10^7$ V/m in Fig. 6(a). One can see that $|\psi_{\uparrow}(k_{x\uparrow},z,y)|^2_{n=1}$ mainly distributes at the top wall surface (x–y plane), and there is a small quantity of distributions of the density at the other three wall surfaces, while $|\psi_{\downarrow}(k_{x\downarrow},z,y)|^2_{n=1}$ almost locates at the bottom wall surface (x–y plane). The dissymmetrical distribution between $|\psi_{\uparrow}(k_{x\uparrow},z,y)|^2_{n=1}$ and $|\psi_{\downarrow}(k_{x\downarrow},z,y)|^2_{n=1}$ at the wall surfaces of the nanoribbon is due to the Rashba spin splitting. With the increase of the electric field, the density $|\psi_{\uparrow}(k_{x\uparrow},z,y)|^2_{n=1}$ gradually gathers at the top wall surface, while $|\psi_{\downarrow}(k_{x\downarrow},z,y)|^2_{n=1}$ still gathers at the bottom wall surface (see Figs. 6(a)–(6c)), which indicates that the wave functions of spin-up and spin-down surface states are gradually separated. When $E_z = 3.75\times10^7$ V/m, the gap is removed as shown in Fig. 1(b), and the densities $|\psi_{\uparrow}(k_{x\uparrow},z,y)|^2_{n=1}$ and $|\psi_{\downarrow}(k_{x\downarrow},z,y)|^2_{n=1}$ are completely separated and respectively distribute at the top and bottom wall surfaces.

Further increasing the electric field, both the densities $|\psi_{\uparrow}(k_{x\uparrow},z,y)|^2_{n=1}$ and $|\psi_{\downarrow}(k_{x\downarrow},z,y)|^2_{n=1}$ distribute at the bottom surface, as shown in Fig. 6(d). Physically, this distinct behavior can be understood as the combined effect of the two forces which act on electrons: one is the SOC force and the other is the electric field one.[32] The directions between the two forces acting on spin-up electrons are opposite, while the two forces act on the spin-down electrons with the same direction (along $-z$ direction). Therefore, with the increase of the electric field, the electric field force gradually increases. When the force is larger than the SOC one, the density $|\psi_{\uparrow}(k_{x\uparrow},z,y)|^2_{n=1}$ shifts from the top wall surface to the bottom wall surface. The density $|\psi_{\downarrow}(k_{x\downarrow},z,y)|^2_{n=1}$ still stays at the bottom surface due to the two forces acting on the spin-down electrons along the $-z$

direction.

We also plot the density distribution $|\psi_{\uparrow\downarrow}(k,z,y)|^2_{n=1}$ of the nanoribbon in the presence of the electric field E_y in the lower panel of Fig. 6. The parameters of the nanoribbon are the same as those of the upper panel of the figure. When $E_y = 1\times10^7$ V/m, the densities $|\psi_{\uparrow}(k,z,y)|^2_{n=1}$ and $|\psi_{\downarrow}(k,z,y)|^2_{n=1}$ mainly distribute at the left and right side surface (z–x plane), respectively. A small quantity of densities $|\psi_{\uparrow}(k,z,y)|^2_{n=1}$ and $|\psi_{\downarrow}(k,z,y)|^2_{n=1}$ distribute at the other three wall surfaces, respectively. With the increase of the electric field E_y, the densities $|\psi_{\uparrow}(k,z,y)|^2_{n=1}$ and $|\psi_{\downarrow}(k,z,y)|^2_{n=1}$ gradually gather at the left and right side surfaces, respectively. When $E_y = 2.7\times10^7$ V/m, the gap closes, and the density $|\psi_{\uparrow\downarrow}(k,z,y)|^2_{n=1}$ only distributes at the left or right side surface, as shown in Fig. 6(g), which indicates that electron states change into helical surface states. Further increasing of the electric field, the gap reopens and a small quantity of densities redistribute at other surfaces (see Fig. 6(h)).

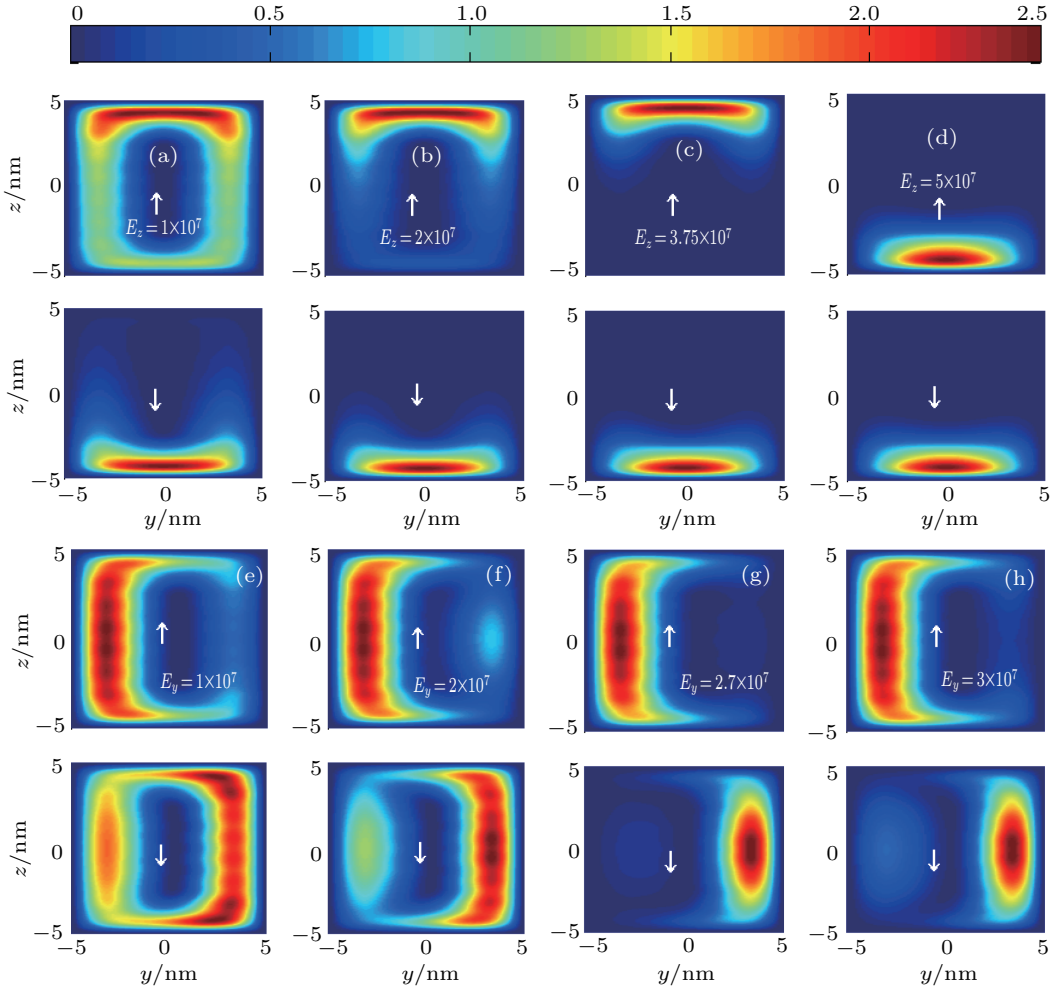


Fig. 6. (color online) Contour plots of the density distributions $|\psi_{\uparrow\downarrow}(k,z,y)|^2_{n=1}$ for a rectangular cross section of a Bi_2Se_3 nanoribbon under different electric fields at $\varepsilon = 90$ meV. On the upper panel, $E_z =$ (a) 1×10^7, (b) 2×10^7, (c) 3.75×10^7, and (d) 5×10^7 V/m. On the lower panel, $E_y =$ (e) 1×10^7, (f) 2×10^7, (g) 2.7×10^7, and (h) 3×10^7 V/m.

Finally, we investigate the transport property of a prism-shaped nanoribbon with $L_z = L_y = 10$ nm under the control of electric fields E_z and E_y, as shown in Fig. 7(a). In order to open the surface channels and provide spin-up and -down Dirac surface states being respectively distributed on top and bottom wall surfaces in two electrodes of the nanoribbon, a fixed electric field E_z along the z direction is applied perpendicularly to the two electrodes. At the same time, a turnable electric field E_y along the y direction is applied perpendicularly to the side wall surfaces of the nanoribbon. The field E_y can adjust the energy gap of the nanoribbon and switch on/off the channels of surface states. We first set the electronic energy $\varepsilon = 90$ meV, which is just in the gap, indicating that there is no electron state in the nanoribbon without an electric field. We plot the spin-dependent conductances as a function of the transverse electric field E_y in Fig. 7(b), where, $G_{\text{total}} = G_{\downarrow\downarrow} + G_{\uparrow\downarrow} + G_{\uparrow\uparrow} + G_{\downarrow\uparrow}$ is the total conductance of the system, and the spin-dependent conductance $G_{\sigma\sigma'}$ is the conductance of electrons injected with spin σ and scattered into states with spin σ'. With the increase of the E_y, the energy gap decreases. The channels for spin-up and -down electrons is switched on at $E_y = 2\times10^6$ V/m, where $e^2/h < G_{\text{total}} < 2e^2/h$. Further increasing of the electric field E_y, the G_{total} gradually decreases and tends to 1, while $G_{\downarrow\downarrow}$ almost remains un-

changed, $G_{\downarrow\downarrow} \approx 1$. In particular, when $E_y > 1.5 \times 10^7$ V/m, $G_{\text{total}} = G_{\downarrow\downarrow}$ and all other conductances $G_{\uparrow\downarrow}$, $G_{\uparrow\uparrow}$, and $G_{\downarrow\uparrow}$ are zero, indicating that the channel for the spin-up surface state closes and the one for the spin-down surface state is still open. The reasons are as follows. With the increase of electric field E_y, the stimulated electronic states gradually turn into helical surface states, as shown in Fig. 6(e)–6(h). The reflection and refraction behaviors of the Dirac electron at the interface between the x–y plane (top and bottom wall surfaces of the left electrode) and the z–x plane (side wall surfaces of the nanoribbon) are similar to optics.[34] Due to the Rashba SOC, the difference of wave vectors between the left electrode and the nanoribbon may result in reflection and refraction. The spin-up wave vectors of the x–y plane in the two electrodes of the nanoribbon are always much larger than those of the z–x plane in the nanoribbon when $E_y < 2.7 \times 10^7$ V/m at $\varepsilon = 90$ meV, as shown in Figs. 2(b) and 2(c). So the phenomenon of total reflection happens easily at the interface between the left electrode and the nanoribbon for spin-up Dirac electrons. That is to say, the spin-up Dirac electrons can be completely blocked when the difference of the vectors between the left electrode and the nanoribbon is large enough by modulation of an appropriate electric field E_y. However, the values of the spin-down wave vectors in the electrode and the nanoribbon are very close, as shown in Figs. 2(b) and 2(c). Therefore, almost all the spin-down Dirac electrons always penetrate the system, but all the spin-up Dirac electrons are always blocked under an appropriate electric field. We also plot the conductance G_{total} at two other fixed energies $\varepsilon = 92$ and 95 meV, which are not in the gap, indicating that there are electron states at the two electron energies. So the charges channels are switched on when $E_y = 0$, as shown in Fig. 6(c). In addition, a similar phenomenon happens for the electron at the energy $\varepsilon = 92$ and 95 meV. With increase of the field E_y, G_{total} first increase and then reduce to e^2/h, indicating that the spin-up electrons are also blocked and only the channel for spin-down electrons is still open. So the spin polarization can be 100% by modulating the E_y in the system. The spin filtering effect does not rely on a tunable Rashba SOC, but on the energy of the edge state, which is similar to the spin switching in a constriction made of the topological insulator mercury telluride (HgTe).[35]

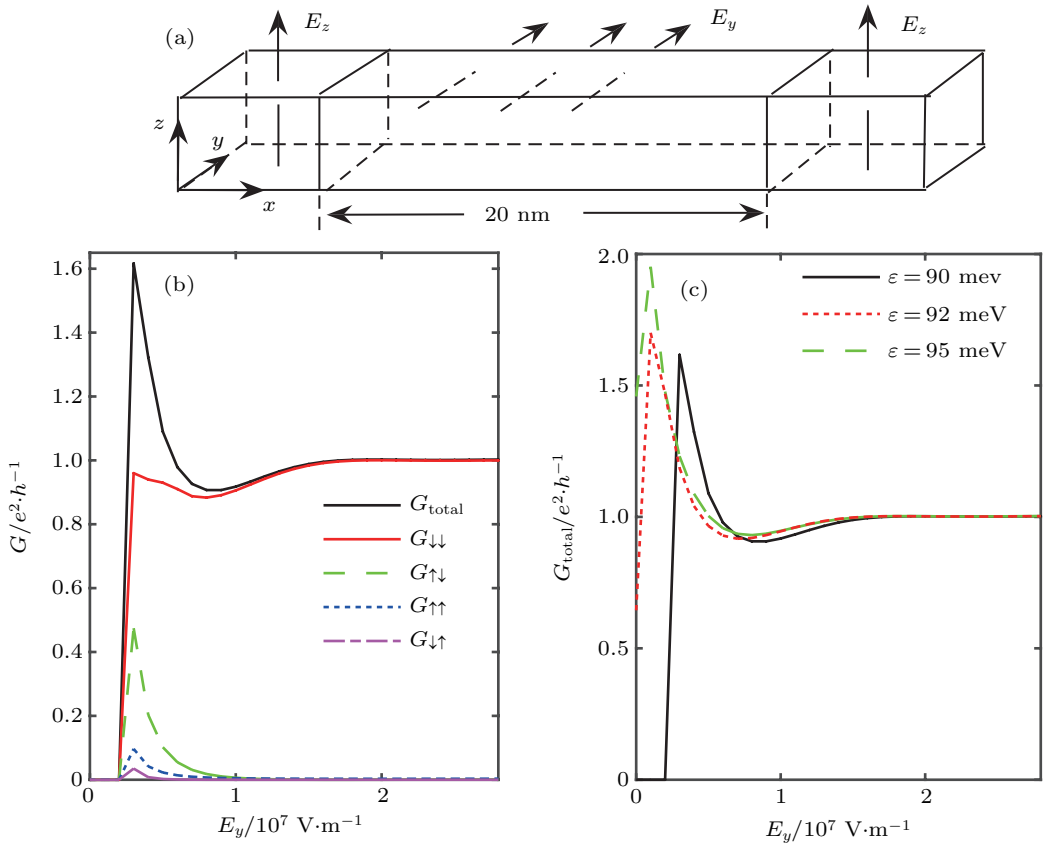


Fig. 7. (color online) (a) Schematic of the nanoribbon. A fixed electric field E_z is perpendicular to the two ends of the nanoribbon, and a turnable electric field E_y is perpendicular to the intermediate section of the nanoribbon. (b) The conductances of the Bi_2Se_3 nanoribbon as a function of E_y at $\varepsilon = 90$ meV. (c) G_{total} of the nanoribbon as a function of E_y at $\varepsilon = 90$, 92, and 95 meV, respectively.

4. Conclusion

We have studied the band structure, electronic density distribution, and electronic transport for a Bi_2Se_3 nanoribbon. We have found that the electric field can eliminate the coupling between surface states in the walls of the nanoribbon, remove the gap of the surface states, and restore the quantum spin Hall effects. We demonstrated that the distribution of the electron states is dependent on the shape and size of

the transverse cross section of the nanoribbon, and the energy of the electron. The surface states can exhibit properties of two-dimensional TI when the energy of the Dirac electron is below the Dirac cone or under an appropriate electric field. In addition, we have studied the spin-dependent transport property of the surface states transmitting from top and bottom surfaces (x–y plane) to the side surfaces (z–x plane) of a Bi_2Se_3 nanoribbon. We have found that the Dirac electrons can exhibit the properties of photons under the modulation of an electric field. We have demonstrated that a transverse electric field can open two surface channels for spin-up and -down Dirac electrons, and switch off one of them for the Dirac electron with one spin orientation. Our results may provide a simple way for the design of a spin filter based on topological insulator nanostructures.

References

[1] Hasan M Z and Kane C L 2010 *Rev. Mod. Phys.* **82** 3045
[2] Miao M S, Yan Q, Van de Walle C G, Lou W K, Li L L and Chang K 2012 *Phys. Rev. Lett.* **109** 186803
[3] Zhang D, Lou W K, Miao M S, Zhang S C and Chang K 2013 *Phys. Rev. Lett.* **111** 156402
[4] Wu Z, Zhai F, Peeters F M, Xu H Q and Chang K 2011 *Phys. Rev. Lett.* **106** 176802
[5] Chang K and Lou W K 2011 *Phys. Rev. Lett.* **106** 206802
[6] He K, Ma X C, Chen X, Lü L, Wang Y Y and Xue Q K 2013 *Chin. Phys. B* **22** 067305
[7] Wang J, Wang N, Huang H and Duan W 2016 *Chin. Phys. B* **25** 117313
[8] Qi X L and Zhang S C 2011 *Rev. Mod. Phys.* **83** 1057
[9] Zhu J J, Yao D X, Zhang S C and Chang K 2011 *Phys. Rev. Lett.* **106** 097201
[10] Tang H, Liang D, Qiu R L J and Gao X P A 2011 *ACS Nano* **5** 7510
[11] Li Y, Wan Q, Peng Y Z, Wang G Q, Qian Z H, Zhou G H and Jalil M B A 2015 *Sci. Rep.* **5** 18458
[12] Li Y, Wan Q and Jalil M B A 2015 *J. Phys. D-Appl. Phys.* **48** 465304
[13] Zhang G, Qin H, Teng J, Guo J, Guo Q, Dai X, Fang Z and Wu K 2009 *Appl. Phys. Lett.* **95** 053114
[14] Xie M H, Guo X, Xu Z J and Ho W K 2013 *Chin. Phys. B* **22** 068101
[15] Kong D, Randel J C, Peng H, Cha J J, Meister S, Lai K, Chen Y, Shen Z X, Manoharan H C and Cui Y 2010 *Nano Lett.* **10** 329
[16] Zhang K, Pan H, Wei Z, Zhang M, Song F, Wang X and Zhang R 2017 *Chin. Phys. B* **26** 096101
[17] Peng H, Lai K, Kong D, Meister S, Chen Y, Qi X L, Zhang S C, Shen Z X and Y Cui 2010 *Nat. Mater.* **9** 225
[18] Linder J, Yokoyama T and Sudbø A 2009 *Phys. Rev. B* **80** 205401
[19] Lu H Z, Shan W Y, Yao W, Niu Q and Shen S Q 2010 *Phys. Rev. B* **81** 115407
[20] Liu C X, Zhang H J, Yan B, Qi X L, Frauenheim T, Dai X, Fang Z and Zhang S C 2010 *Phys. Rev. B* **81** 041307(R)
[21] Fu Z G, Zhang P and Lee S S 2011 *Appl. Phys. Lett.* **99** 243110
[22] Hao L, Thalmeier P and Lee T K 2011 *Phys. Rev. B* **84** 235303
[23] Egger R, Zazunov A and Yeyati A L 2010 *Phys. Rev. Lett.* **105** 136403
[24] Lou W K, Cheng F and Li J 2011 *J. Appl. Phys.* **110** 093714
[25] Zhang Y, He K, Chang C Z, Song C L, Wang L L, Chen X, Jia J F, Fang Z, Dai X, Shan W Y, Shen S Q, Niu Q, Qi X L, Zhang S C, Ma X C and Xue Q K 2010 *Nat. Phys.* **6** 584
[26] Zhang T, Ha J, Levy N, Kuk Y and Stroscio J 2013 *Phys. Rev. Lett.* **111** 056803
[27] Imura K I, Okamoto M, Yoshimura Y, Takane Y and Ohtsuki T 2012 *Phys. Rev. B* **86** 245436
[28] Qu D X, Hor Y S, Xiong J, Cava R J and Ong N P 2010 *Science* **329** 821
[29] Xiu F, He L, Wang Y, Cheng L, Chang L T, Lang M, Huang G, Kou X, Zhou Y, Jiang X, Chen Z, Zou J, Shailos A and Wang K L 2011 *Nat. Nanotechnol.* **6** 216
[30] Zhang H, Liu C X, Qi X L, Dai X, Fang Z and Zhang S C 2009 *Nat. Phys.* **5** 438
[31] Zhang L B, Cheng F, Zhai F and Chang K 2011 *Phys. Rev. B* **83** 081402(R)
[32] Liu G H, Zhou G H and Chen Y H 2011 *Appl. Phys. Lett.* **99** 222111
[33] Zhang L, Zhuang J N, Xing Y X, Li J, Wang J and Guo H 2014 *Phys. Rev. B* **89** 245107
[34] Moon C Y, Han J, Lee H and Choi H J 2011 *Phys. Rev. B* **84** 195425
[35] Krueck V and Richter K 2011 *Phys. Rev. Lett.* **107** 086803